

# Optimal Color Composition Method for Generating High-Quality Daily Photographic Time Series From PhenoCam

Qing Li, Miaogen Shen<sup>1</sup>, Xuehong Chen<sup>2</sup>, Cong Wang, Jin Chen, Xin Cao<sup>3</sup>, and Xihong Cui

**Abstract**—Phenology camera (PhenoCam) data and the derived green chromatic coordinate (GCC) time series are commonly used to track seasonal changes in canopy greenness. However, the GCC time series is noisy because color distortion commonly exists in the captured photographs owing to the varying illumination conditions and nonlinear response of the consumer-grade camera to the incoming light. Hence, we proposed an optimal color composition (OCC) method to generate high-quality daily photographic time series by compositing multiple photographs captured in a single day. First, the optimal acquisition time with good illumination conditions and correct exposure settings is determined for each pixel throughout the day based on a comprehensive color index, combining the brightness and saturation. A virtual photograph consisting of the selected digital numbers acquired at the optimal time is then composited for each day. Finally, the daily GCC time series is calculated based on the virtual photographs. By testing the photographs of six forest sites, the proposed method was compared with the commonly used 90th percentile (Per90) filter. The results show that the daily photographs composited using the OCC method were more homogeneous with less shaded areas compared to those selected by the Per90 filter, and the corresponding GCC time series derived from the OCC method is more stable and less influenced by varying atmospheric conditions and solar angles than the Per90 filter. These results indicate that the OCC method can generate

high-quality daily photographic time series with the potential to better indicate seasonal color changes in the forest canopy.

**Index Terms**—Green chromatic coordinate (GCC), optimal color composition (OCC), PhenoCam.

## I. INTRODUCTION

VEGETATION phenology, referring to seasonality or periodic biological phenomena, has attracted significant attention owing to its sensitivity to climate change and various feedback to the climate system [1]. Traditionally, there are two ways to conduct a phenological observation: human observation in the field and remote sensing observation. Human observations in the field primarily document key phenological events in the life cycle of individual plants, such as budburst, flowering, and leaf coloring [2]. However, such observations lack objectivity and continuity, leading to difficulty in guaranteeing data consistency across time and space [3], [4] and in reflecting continuous phenological development [5]–[7]. Remote sensing provides an objective and continuous method for phenological observation; however, it is typically influenced by serious data noise (e.g., cloud contamination [8], [9] or the snow effect [10], [11]), mixed pixel effect [12]–[14], and uncertainty among the different phenological detection methods [15].

The use of a phenology camera (PhenoCam), as a supplementary observation tool at the canopy scale [16], has recently become increasingly popular in various studies. PhenoCam is a type of consumer-grade red–green–blue (RGB) digital camera set up at a fixed location to capture time-lapse photographs. Typically, photographs are repeatedly captured with a frequency of 30 min or 1 h during a long-term period. Thus, PhenoCam records the growth status of the vegetation within a photographic scene in a continuous and objective manner. Owing to their low cost, convenient layout, and high observation frequency, PhenoCam networks have been established worldwide [17]–[19], and the data have become an integral long-term data source in numerous application fields [19]. For example, the time series of the green index derived from PhenoCam photographs has widely been used for identifying key phenological events [20]–[22] as well as to validate land surface phenology products of remote sensing [23]–[26]. PhenoCam data also help reveal the impact of short-term disturbances or management measures under vegetation growth conditions, including species invasion [27], burning, harvesting, and grazing [28], along with biological and

Manuscript received April 7, 2021; revised May 21, 2021; accepted May 26, 2021. Date of publication June 10, 2021; date of current version June 29, 2021. This work was supported in part by the National Natural Science Foundation of China under Project 41871224, in part by the Faculty Start-Up Fund of Beijing Normal University, in part by the Key Research Program of Frontier Sciences under Grant QYZDB-SSW-DQC025, in part by the Youth Innovation Promotion Association of the Chinese Academy of Sciences, in part by the Top-Notch Young Talents Program of China, in part by the U.S. National Park Service Inventory and Monitoring Program and the USA National Phenology Network under Grant G10AP00129 from the United States Geological Survey and the USA National Phenology Network and North Central Climate Science Center under Cooperative Agreement G16AC00224 from the United States Geological Survey, and in part by the National Science Foundation's LTER Program for research at Harvard Forest under Grant DEB-1237491 and Bartlett Experimental Forest under Grant DEB-1114804. (Corresponding author: Miaogen Shen.)

Qing Li, Xuehong Chen, Jin Chen, Xin Cao, and Xihong Cui are with the State Key Laboratory of Remote Sensing Science, Institute of Remote Sensing Science and Engineering, Faculty of Geographical Science, Beijing Normal University, Beijing 100875, China (e-mail: liqing1106@mail.bnu.edu.cn; chenxuehong@bnu.edu.cn; chenjin@bnu.edu.cn; caoxin@bnu.edu.cn; cuixihong@bnu.edu.cn).

Miaogen Shen is with the Institute of Land Surface System and Sustainable Development, Faculty of Geographical Science, Beijing Normal University, Beijing 100875, China (e-mail: shenmiaogen@bnu.edu.cn).

Cong Wang is with the Key Laboratory of Agricultural Remote Sensing, Ministry of Agriculture and Rural Affairs/Institute of Agricultural Resources and Regional Planning, Chinese Academy of Agricultural Sciences, Beijing 100081, China (e-mail: wangcong01@casa.cn).

Digital Object Identifier 10.1109/JSTARS.2021.3087814

abiotic stress events [29]. Moreover, PhenoCam data have shown potential for modeling seasonal changes in the gross primary production [30] and leaf biochemical/biophysical parameters [31].

However, as a consumer-grade camera, PhenoCam captures photographs stored in digital numbers (DNs), which lack precise radiometric calibration [19]. Owing to the variability of illumination conditions (changing atmospheric conditions and solar angle) and inconsistency of internal factors (e.g., exposure setting, white balance program, and nonlinear response curve of incoming light), the photographs captured at different times on the same day could show large differences in color [32]. Therefore, the DN time series of RGB channels is extremely noisy and can rarely be directly used for phenological analysis [16], [33]. To suppress the errors caused by the above factors, the DNs of the RGB bands were typically converted into chromatic coordinates [34]. Green chromatic coordinates (GCCs) have become the most widely used index to characterize the seasonal trajectory of vegetation color and physiological activity [16]. Although the inherent errors caused by the camera, such as the exposure time and white balance, can relatively be alleviated through the ratio form of GCC, the variation in atmospheric conditions (sunny/cloudy), and solar angle largely affect the stability of a GCC time series. For example, varying atmospheric conditions alter the proportion of scattered light, leading to a color difference between the photographs captured under sunny and cloudy atmospheric conditions. The shadow area within the observation scene also changes with the varying solar angle; thus, the GCC value can change with the daily and seasonal changes in the solar angle. Moreover, the response of incoming light is typically nonlinear for a consumer-grade camera, which further increases the color distortion of the captured photographs under varying illumination conditions. Various methods have been employed to reduce the data noise in the GCC time series. Julitta *et al.* [35] designed a threshold based on the blue chromatic coordinates to exclude the GCC of photographs captured under poor weather conditions, considering that scattered light can significantly alter the DN value of the blue channel. Filippaa *et al.* [36] employed an outlier detection method based on a double-difference time series to filter the GCC time series. Migliavacca *et al.* [30] used recursive spline smoothing and residual calculations to remove outliers outside the envelope of the residual. Sonnentag *et al.* [34] smoothed the GCC time series by taking the 90th percentile of all daytime GCC values within a certain time window (1 or 3 days). Owing to its simplicity and convenience, the 90th percentile filter (hereafter referred to as Per90) has become the most widely used method in the preprocessing of GCC time series [35], [37]. However, these methods reduce the noise in GCC time series through statistical criteria without directly considering the photographic color distortion induced by varying illumination conditions and nonlinear camera response of incoming light. Although the standard ColorChecker charts at a few sites can help in correcting the color of photographs [38], they are still lacking in most of the PhenoCam sites because of the difficulty in effective field maintenance.

In summary, few method has been developed for calibrating PhenoCam photographs by considering the color distortion induced under varying illumination conditions and a nonlinear response to incoming light. To address this issue, this study aims to design an optimal color composition (OCC) method for generating high-quality daily photographic time series from PhenoCam. As the illumination condition varies spatially and temporally, the optimal acquisition time with good illumination conditions and correct exposure settings can be determined for each pixel throughout a single day based on a certain color criterion. A virtual photograph consisting of the selected DNs acquired at the optimal time is then composited for each day. The time series of the composited photographs are expected to be insensitive to varying solar angles and atmospheric conditions, from which a more stable GCC time series can be derived compared with the existing methods.

## II. MATERIALS AND METHODS

### A. PhenoCam Photographs

In this study, PhenoCam photographs captured in three deciduous broad-leaved forest sites and three evergreen coniferous forest sites were used to test the performance of the proposed composition method. The six stations include the two main types of forest vegetation located in different climate zones with different atmospheric conditions and sun trajectories. Detailed information about the experimental sites is presented in Table I, and sample photographs are shown in Fig. 1. The PhenoCam photographs in these six sites are 3-megapixel RGB photographs in JPEG format. The white balance and exposure time were determined automatically using the site cameras. The capturing interval of the PhenoCams at the selected sites was 30 min, except for the Niwot2 site where the photographs were captured every 15 min. Considering the sunrise and sunset times at each site, only the photographs captured between 09:00 and 15:00 local time were considered in this study.

### B. Optimal Color Composition

The DN value of the PhenoCam photographs is largely influenced by the varying atmospheric conditions and solar angles. Although the correction of atmospheric and solar angle effects on satellite imagery has been well explored in the remote sensing community [39]–[42], it is difficult to establish an effective physical bidirectional reflectance distribution function model or atmospheric correction method for PhenoCam photographs because of the lack of proper radiometric calibration and canopy structure models at a small scale. Typically, the pixel color is close to the true color when it is captured under good illumination conditions and with suitable exposure settings. However, because of the inevitable shadow areas in the photographs, the exposure time of an entire photograph is unsuitable for all the pixels in the photographic scene. The shadow pixels in one photograph are typically underexposed, whereas some extremely bright pixels are overexposed. Considering the varying illumination conditions throughout the day, the locations of the shadow and bright pixels also correspondingly change.

TABLE I  
PHENOCAM FOREST STUDY SITES

Site Name	Location	Lat.; long. (°; °)	Elev. (m ASL)	Forest type	Dominant species	Year	Interval; temporal coverage
Alligatorriver <sup>a</sup>	Alligator River National Wildlife Refuge, North Carolina	35.79; -75.90	1	DB	<i>Nyssa sylvatica</i> , <i>Taxodium distichum</i> <i>Nyssa aquatica</i> , <i>Acer rubrum</i>	2014	hh; 07:30–19:30
Bartlettir <sup>b</sup>	Bartlett Experimental Forest, Bartlett, New Hampshire	44.06; -71.29	268	DB	<i>Acer rubrum</i> , <i>Betula papyrifera</i> , <i>Fagus grandifolia</i>	2019	hh; 06:00–19:30
Howland1 <sup>c</sup>	Main Tower (Mature stand), Howland Forest, Howland, Maine	45.20; -68.74	80	EN	<i>Picea rubens</i> , <i>Tsuga canadensis</i> , <i>Acer rubrum</i>	2016	hh; 06:00–18:00
Millhaft	Norbury, Staffordshire, UK,	52.80; -2.30	137	DB	<i>Quercus petraea</i>	2018	hh; 04:00–23:30
Niwot2 <sup>d</sup>	Niwot Ridge Mountain Research Station, Roosevelt National Forest, Colorado	40.03; -105.55	3050	EN	<i>Picea engelmannii</i> , <i>Abies lasiocarpa</i> , <i>Pinus contorta</i>	2014	15 min; 04:00–22:00
OregonMP <sup>e</sup>	Metolius intermediate pine/US- Me2, near Sisters, Oregon	44.45; -121.56	1253	EN	<i>Pinus ponderosa</i>	2016	hh; 04:00–22:30

Forest types are DB = deciduous broad-leaved forest, EN = evergreen needle-leaved forest. Intervals are 15 min, half-hourly (hh) or hourly (h).

<sup>a</sup>Supported by DOE NICCR (award 08-SC-NICCR-1072), DOE-TES (awards 11-DE-SC-0006700 and 7090112), USDA Forest Service (award 13-JV-11330110-081), and USDA-NIFA (award 2014-67003-22068).

<sup>b</sup>Supported by the National Science Foundation (grant DEB-1114804) and the USDA Forest Service's Northern Research Station.

<sup>c</sup>Supported by the Office of Science (BER), U.S. Department of Energy, and the USDA Forest Service's Northern Research Station.

<sup>d</sup>Supported by the U.S. DOE, Office of Science through the AmeriFlux Management Project (AMP) at Lawrence Berkeley National Laboratory under Award Number 7094866.

<sup>e</sup>Provided from the Metolius Core Site Cluster by the DOE Office of Science AmeriFlux Network Management Project.

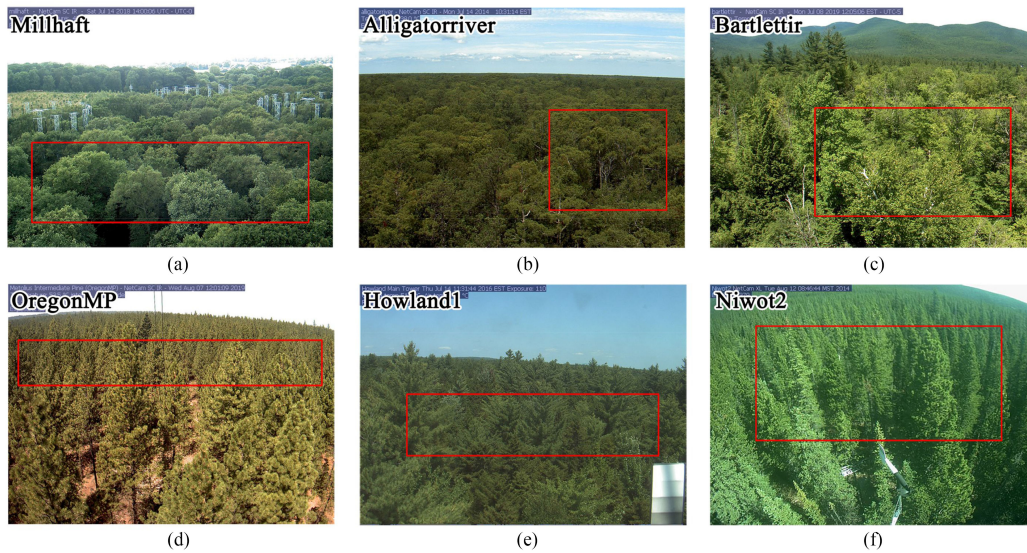


Fig. 1. Photographs acquired by PhenoCams at six sites. The red polygons indicate the ROIs used for extracting the GCC time series.

Thus, by selecting the DN acquired in the optimal time with good illumination conditions and correct exposure settings for each pixel throughout a single day, a virtual photograph without excessively dark or bright pixels can be composited for each day. Brightness and color saturation can largely reflect whether the pixel is well illuminated and exposed correctly and were used as the main criteria for determining the optimal acquisition time for each pixel. As shown in Fig. 2, the proposed OCC

method primarily consists of three steps: a hue–saturation–value (HSV) transformation, optimal DN selection and composition, and GCC calculation in a predefined region of interest (ROI).

1) *HSV Transformation*: To acquire information regarding color brightness and saturation, the RGB color mode in the original PhenoCam photographs is transformed into the HSV mode. The corresponding three color components, hue (H),



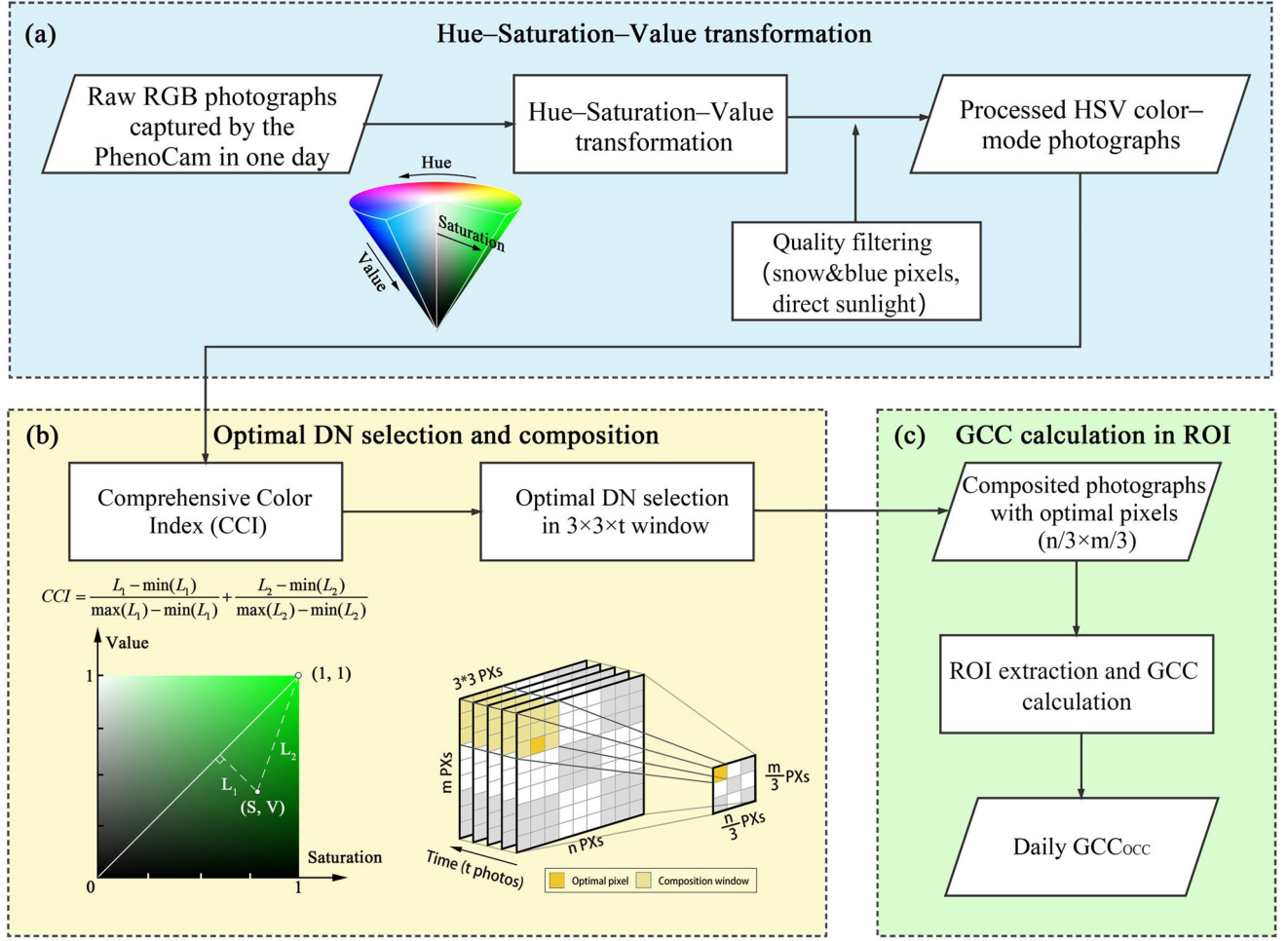


Fig. 2. Flowchart of OCC method with three steps. (a) Hue-saturation-value transformation. (b) Optimal DN selection and composition. (c) GCC calculation in ROI.

saturation (S), and value (V), are calculated as follows [43]:

$$H = \begin{cases} \text{Undefined} & \text{if } DN_{\max} = DN_{\min} \\ 60^\circ \times \frac{G-B}{DN_{\max}-DN_{\min}} + 0^\circ, & \text{if } DN_{\max} = R \text{ and } G \geq B \\ 60^\circ \times \frac{G-B}{DN_{\max}-DN_{\min}} + 360^\circ, & \text{if } DN_{\max} = R \text{ and } G < B \\ 60^\circ \times \frac{B-R}{DN_{\max}-DN_{\min}} + 120^\circ, & \text{if } DN_{\max} = G \\ 60^\circ \times \frac{R-G}{DN_{\max}-DN_{\min}} + 240^\circ, & \text{if } DN_{\max} = B \end{cases}$$

$$S = \begin{cases} 0, & \text{if } DN_{\max} = 0 \\ 1 - \frac{DN_{\min}}{DN_{\max}}, & \text{otherwise} \end{cases}$$

$$V = DN_{\max}$$

(1)

where  $R$ ,  $G$ , and  $B$  are the DNs of the red, green, and blue channels for each pixel, ranging from 0 to 255; and  $DN_{\max}$  and  $DN_{\min}$  denote the maximum and minimum DNs among  $R$ ,  $G$ , and  $B$  for each pixel, respectively. For HSV mode, hue denotes the color type, ranging from 0 to 360, saturation denotes the color vibrancy, ranging from 0% to 100%, and value denotes the brightness, ranging from 0% to 100%.

Here, some pixels under three particular conditions were excluded because they could not reflect the true color of the vegetation. First, the snow-covered pixels [see Fig. 3(a)] were excluded with a white-color criterion, in which the DNs of

the RGB bands exceed 230. Second, photographs with direct sunlight into the lens [see Fig. 3(b)] were excluded. Direct sunlight photographs were determined using the sun-camera geometry calculated by the local latitude, longitude, capture time, and camera angle. Third, some ordinary blue photographs [see Fig. 3(c)] with hue ranging from 170 to 270 were also excluded because they are far from true vegetation color [35].

2) *Optimal DN Selection and Composition:* To determine the optimal acquisition time when the illumination condition is good and the exposure setting is suitable for each pixel, a comprehensive color index (CCI) that combines value and saturation is proposed

$$CCI = \frac{L_1 - \min(L_1)}{\max(L_1) - \min(L_1)} + \frac{L_2 - \min(L_2)}{\max(L_2) - \min(L_2)}$$

where

$$L_1 = \sqrt{2}/2 |S - V| \text{ and } L_2 = \sqrt{(1 - S)^2 + (1 - V)^2}. \quad (2)$$

Here,  $L_1$  and  $L_2$  represent the color distances from the target pixel to the upper-right corner (1, 1), and from the target pixel to the 1:1 line in the value-saturation space, respectively [see



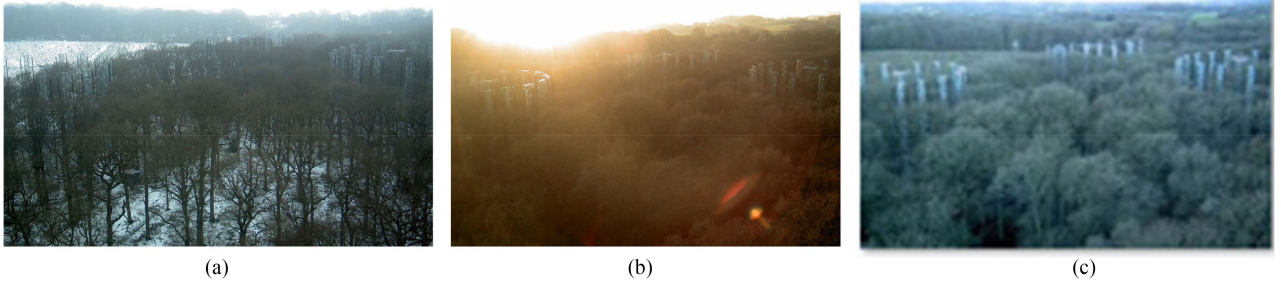


Fig. 3. Examples of photographs that need to be excluded under special circumstances. (a) Snow pixels. (b) Direct solar light. (c) Blue pixels.

Fig. 2(b)]. In addition,  $L_1$  is used to remove extremely bright pixels that are overexposed, whereas  $L_2$  is used to remove the shadow pixels that are underexposed. To further balance the roles of  $L_1$  and  $L_2$ , they are normalized for each day before being summed as CCI. Thus, the sum of normalized  $L_1$  and  $L_2$ , considering both the color saturation and brightness, was used as a comprehensive criterion for determining the optimal acquisition time for each pixel. Because the RGB DN corresponding to a smaller CCI is more likely to be captured under good illumination conditions and correct exposure settings, the optimal acquisition time for each pixel is determined as the one with the minimum CCI throughout a single day.

In addition, to avoid the movement of leaves in the photographs throughout the day, the optimal DNs are selected using a nonoverlapping sliding window of  $3 \times 3$  pixels. Assuming that there were  $t$  photographs with a size of  $n \times m$  pixels in one day, the DNs with the maximum CCI values were selected from a  $3 \times 3 \times t$  nonoverlapping sliding window [see Fig. 2(b)]. Thus, a virtual photograph with a smaller size  $(n/3) \times (m/3)$  is finally composited for each day.

3) *ROI Extraction and GCC Calculation*: Similar to previous studies [19], [34], a single ROI was identified for the photographs of each site (see Fig. 1), with the aim of each ROI containing only target vegetation without sky or other features. Subsequent calculations and analyses were conducted within the ROIs. For each composited virtual photograph, GCC was calculated as follows:

$$GCC_{OCC} = \frac{G_{OCC}}{R_{OCC} + G_{OCC} + B_{OCC}} \quad (3)$$

where  $R_{OCC}$ ,  $G_{OCC}$ , and  $B_{OCC}$  are the mean DNs for the RGB channels of the composite photographs generated by the OCC method. Eventually, a stable  $GCC_{OCC}$  time series throughout the year can be generated without any ancillary data.

### C. Influence of Varying Illumination Conditions on GCC Values

The stability and robustness of the proposed method to varying illumination conditions of the GCC time series were compared with the existing mainstream methods, that is, Per90, which reconstructs the GCC time series by selecting the 90th percentile of all daytime GCC values in one day [32]. Both methods generated photographs and a GCC time series at a daily temporal resolution.

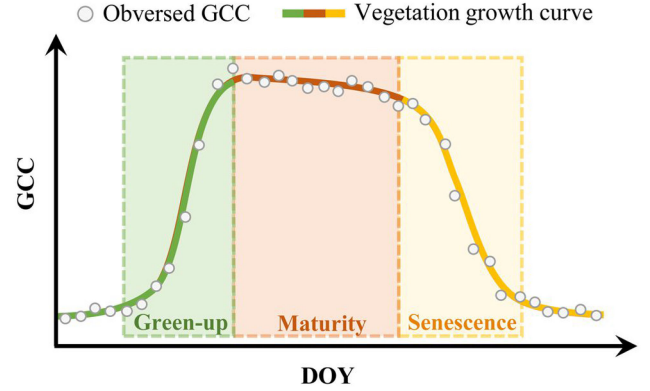


Fig. 4. Schematic of annual GCC trajectory.

1) *Smoothness of Composited GCC Time Series*: To evaluate the stability of the time series, the local coefficient of variation (CV) within a 10-day period was calculated as an indicator of the stability of the GCC time series

$$CV_{local} = \frac{\sqrt{\sum_{i=1}^{10} (GCC_i - \overline{GCC})^2 / 10}}{\overline{GCC}} \quad (4)$$

where  $GCC_i$  is the  $i$ th reconstructed daily GCC during ten days and  $\overline{GCC}$  is the average value of the reconstructed daily GCC in a 10-day window. For the forest, the color and structure of the vegetation canopy typically remained stable within a 10-day period during the maturity period (see Fig. 4). Hence, a more stable algorithm should yield less local variance in the GCC for this time period.

2) *Sensitivity of Generated GCC to Varying Illumination Conditions*: Owing to the lack of reference GCC curves acquired under ideal illumination conditions, in this study, the sensitivity of the generated GCC to varying illumination conditions was evaluated in an indirect manner. As shown in Fig. 5, two subsets of original photographs were resampled to simulate the change in atmospheric conditions and solar angle through which a new GCC time series was generated. The residual between the GCC time series generated from the resampled and original datasets was then used to represent the sensitivity of the generated GCC to varying illumination conditions.

Data from the Millhaft, Alligatorriver, and Bartlettir sites were used to explore the influence of different atmospheric conditions, considering the frequent cloudy days at these sites. Based on our

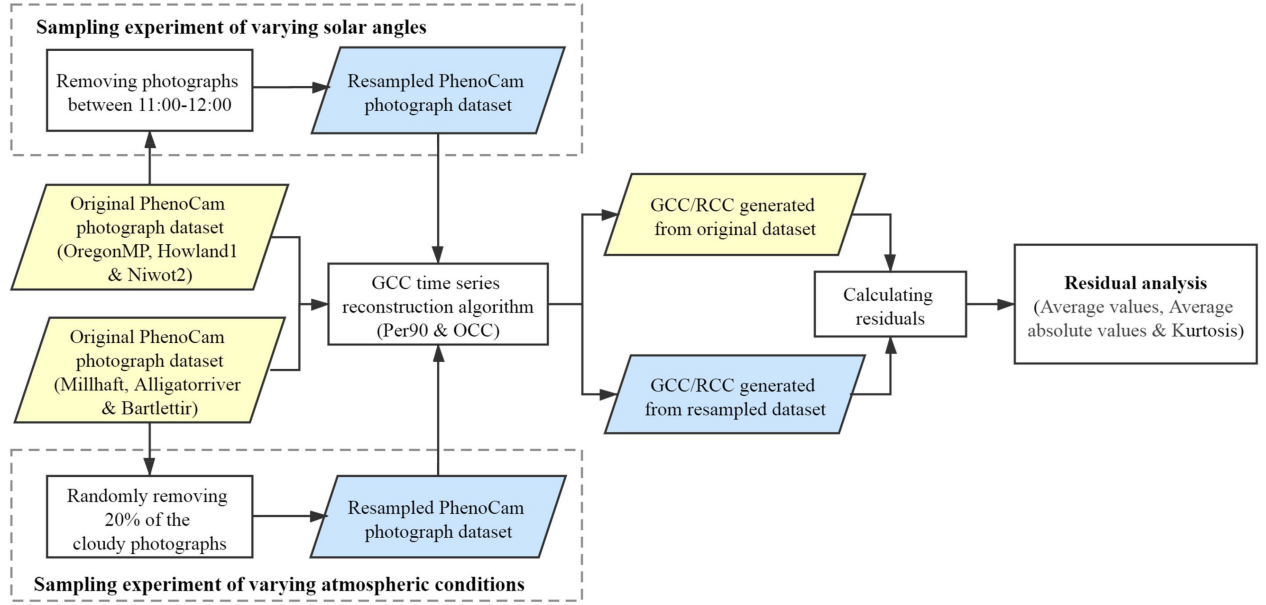


Fig. 5. Flowchart of sampling experiment to evaluate the influence of varying solar angles and atmospheric conditions.

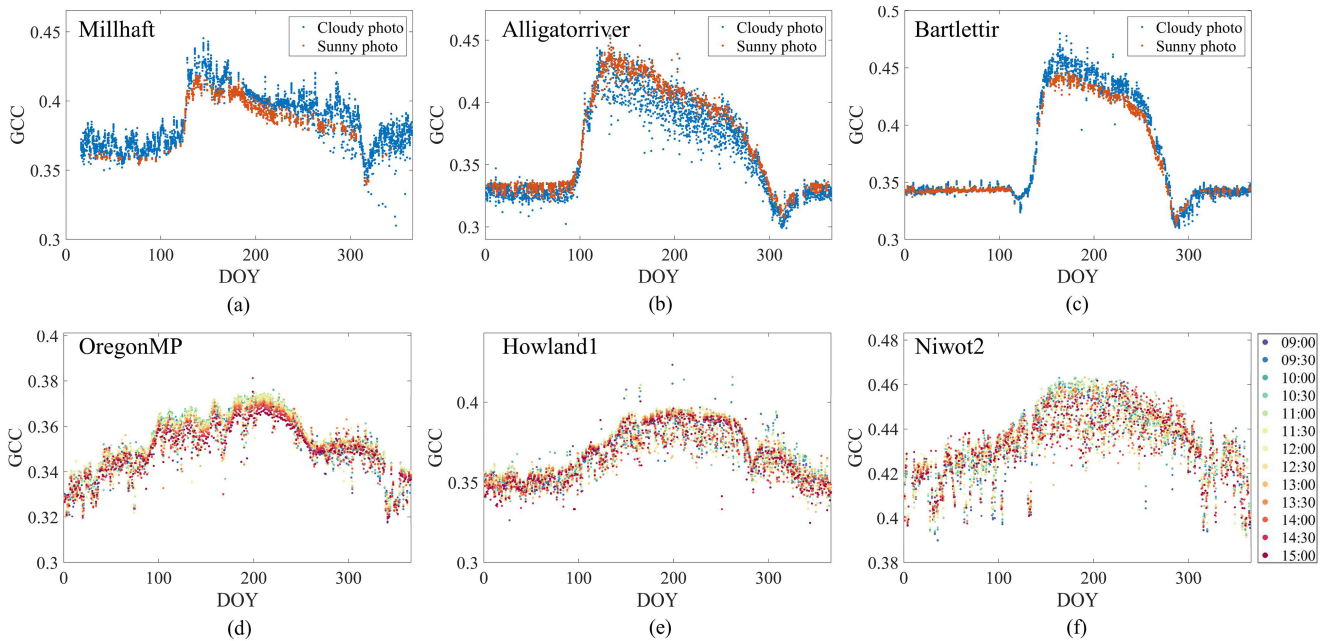


Fig. 6. GCC shows (a)–(c) large differences between sunny and cloudy weather for the sites of Millhaft, Alligatorriver, and Bartlettir; and (d)–(f) time-dependence throughout one day in the sites of OregonMP, Howland1, and Niwot2.

experience, cloudy and sunny photographs can be distinguished by the image contrast, which is calculated as follows:

$$\text{Contrast} = \sum_{\delta} \delta(i, j)^2 P_{\delta}(i, j)^2 \quad (5)$$

where  $\delta(i, j) = |i - j|$  is the grayscale difference between adjacent pixels and  $P_{\delta}(i, j)$  is the probability that the gray-level difference between adjacent pixels is equal to  $\delta$ . In general, photographs with a higher contrast were more likely to be captured on sunny days. Based on our empirical visual observation, the contrast thresholds for distinguishing sunny and

cloudy photographs were set to 0.022, 0.007, and 0.024 for the sites of Millhaft, Alligatorriver, and Bartlettir, respectively. As shown in Fig. 6(a)–(c), there is a significant difference between the GCC values of the sunny and cloudy photographs, confirming that the atmospheric conditions largely influence the GCC values. Based on the labels of sunny and cloudy images determined by the contrast thresholds, a resampled photograph dataset was generated by randomly removing 20% of the cloudy photographs from the original dataset (see Fig. 5). Thus, the resampled dataset could be considered as a simulation of the dataset with less cloudy weather. Two GCC time series were then

generated from the resampled and original datasets. When the residual between two composited GCC time series is smaller, the generation method is considered to be less sensitive to varying atmospheric conditions. To stabilize the results, the experiment was repeated five times. The histogram of the residual between the composited GCC time series from the resampled datasets and the original dataset was plotted, and the average values of the residuals, average absolute values of the residuals, and the kurtosis of the residual distribution were used to represent the sensitivity of the generation method to varying atmospheric conditions.

The data from the OregonMP, Howland1, and Niwot2 sites were used to examine the sensitivity of the generated GCC to different solar angles considering the few cloudy days at these sites. As shown in Fig. 6(d)–(f), GCC exhibits an evident dependence on the acquired time throughout the day. The GCCs derived from photographs captured at noon are typically higher than those derived from photographs captured in the morning or afternoon, which exhibit the solar angle effect on the GCC values. However, it is difficult to directly reflect the influence of the seasonal variation of solar angle on the daily GCC because the seasonal change in vegetation greenness is in some way synchronous with the seasonal change in solar angle. Thus, in this study, we intercepted the PhenoCam data during the summer maturity period when the canopy color remained stable, and removed photographs with a high solar angle (photographs captured at 11:00, 11:30, and 12:00) to simulate the PhenoCam photographs of the same vegetation canopy captured during the winter (see Fig. 5). Thus, the original and resampled datasets could be considered as two datasets acquired during summer and winter, respectively, for the same canopy. Then, two GCC time series were generated from the resampled and original datasets. The average values of the residuals, average absolute values of the residuals, and kurtosis of the residual distribution were also used to represent the sensitivity of the composition method to varying solar angles.

### III. RESULTS

#### A. Virtual Photographs Generated Using OCC

Virtual photographs were generated using the proposed OCC method for each day. Daily photographs corresponding to the Per90 method were also generated for comparison. As shown in Fig. 7, the photographs generated by OCC appear more homogeneous with considerably fewer shadows compared with photographs selected by Per90 in the Millhaft site. The comparison results were similar to the other five sites (see Figs. S1–S5, Supplementary Material). Fig. 8 shows a detailed example during a short period of four days to illustrate the difference between the OCC method and Per90 selection. Among the original photographs, the cloudy photographs (i.e., 14:30 on DOY 138, and 12:30 and 13:30 on DOY 140) were considerably darker than the sunny photographs, leading to a large color variation in the original photographs. The OCC method selected bright pixels to avoid the influence of cloudy atmospheric conditions and produced composited photographs with consistent color during these four days. Contrastingly, the Per90 method failed

to select a sunny photograph and produced an unstable GCC time series because the cloudy photograph on DOY 140 has an unusually high GCC value [see Fig. 8(f)]. Moreover, this example shows the potential to address the solar angle effect for the OCC method. For a sunny day (DOY 139), the area and position of the illuminated and shaded surfaces of the vegetation canopy in the original photographs changed as the solar position changed from 9:30 to 15:00 [see Fig. 8(b)]. The proposed OCC method effectively reduced the most shaded surfaces; thus, it is insensitive to daily changes in the solar angle and is also potentially robust to seasonal changes in this angle. Alternatively, the Per90 method typically selects the photograph captured at noon when there is still a large portion of shaded surfaces that might change with seasonal changes in solar angle.

#### B. Smoothness of Generated GCC Time Series

The local CV during the growing season was calculated to quantify the smoothness of the GCC curve. For the Millhaft, Alligatorriver, and Bartlettir sites, where the atmospheric condition varies greatly, the local CV of  $GCC_{OCC}$  during the maturity period (roughly DOY 150–300) is considerably less than that of  $GCC_{Per90}$  (GCC generated using a Per90 filter) [see Fig. 9(a)–(c)], indicating that the proposed OCC method generates a more stable GCC time series with fewer outliers. For the OregonMP, Howland1, and Niwot2 sites, where the varying solar angle is a dominating inferring factor to GCC values, the proposed method did not show superiority in the stability [see Fig. 9(d)–(f)] because the solar angle also changed smoothly. However, the outliers in the Niwot2 site were removed more effectively by the proposed method. However, the results of the OCC method were more volatile than those of the Per90 method during winter owing to snow contamination. This implies that the simple exclusion of snow-cover pixels when applying this method (see Section II-B1) is inadequate to address the snow effect.

#### C. Sensitivity Analysis of Sampling Experiments

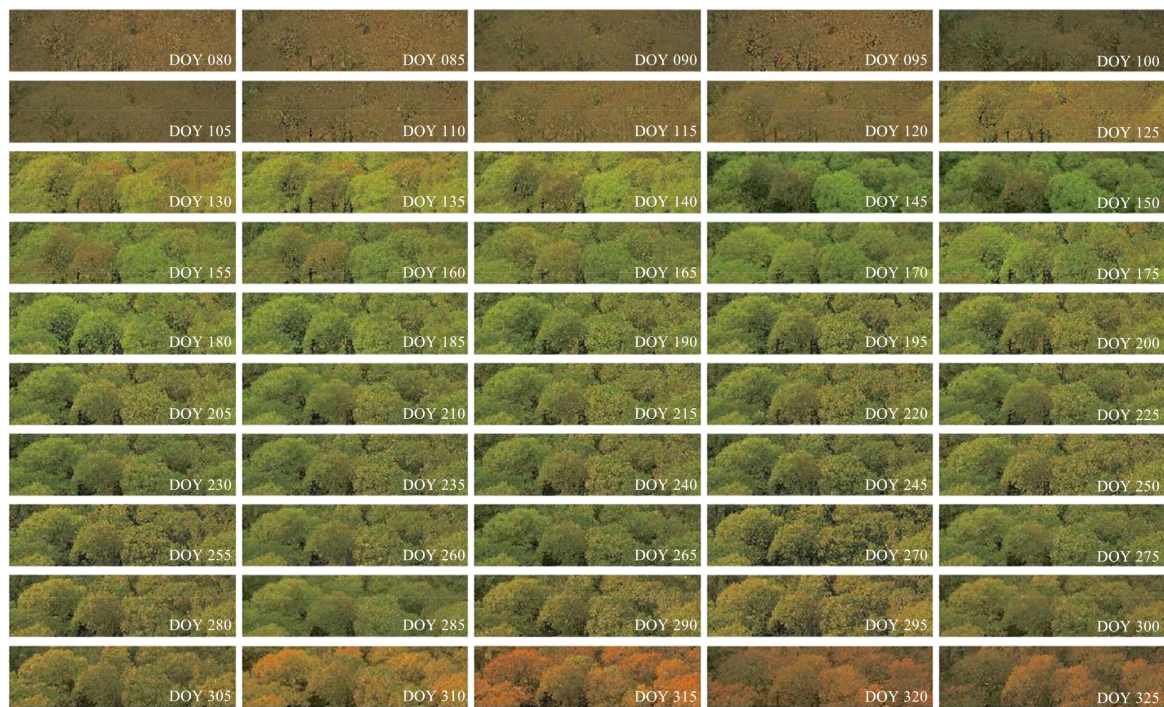
The sampling experiments described in Section II-C2 were conducted to explore the sensitivity of the generated GCC time series to varying solar angles and atmospheric conditions.

At the sites where atmospheric conditions change significantly (i.e., Millhaft, Alligatorriver, and Bartlettir), the histogram of the residuals between the GCC derived from the original and resampled photographs is shown in Fig. 10. The residuals of  $GCC_{OCC}$  exhibit a more concentrated distribution around zero with a smaller bias, smaller mean absolute error, and larger kurtosis (except for Alligatorriver) compared with those of  $GCC_{Per90}$ . These results indicate that the OCC method is less sensitive to atmospheric conditions and hence obtained more stable and relatively unbiased results in the presence of atmospheric changes.

At the sites where changes in the solar angle dominate the GCC noise (i.e., OregonMP, Howland1, and Niwot2), the residuals of  $GCC_{OCC}$  also exhibit a more concentrated distribution around 0 with a smaller bias and mean absolute error compared with those of  $GCC_{Per90}$  (see Fig. 11). This indicates that missing



## Photographic time series generated by OCC



(a)

## Photographic time series generated by Per90



(b)

Fig. 7. (a) Virtual photographs generated using OCC and (b) photographs selected by Per90 for Millhaft site during DOY 80–325. The photographic time series is shown with an interval of five days owing to a limited page length.



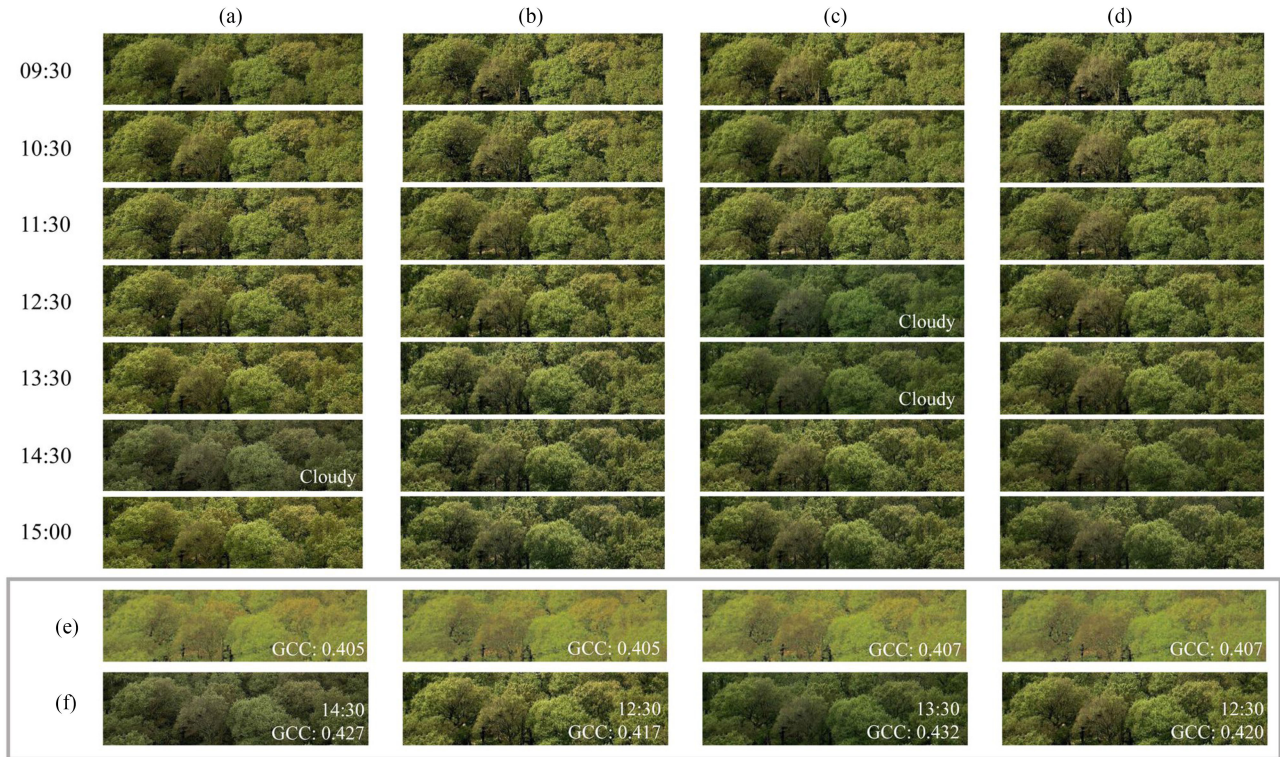


Fig. 8. (a)–(d) Examples of original photographs captured in the deciduous broadleaf site of Millhaft during DOY 138–141, and the daily photographic time series generated by (e) OCC and (f) Per90.

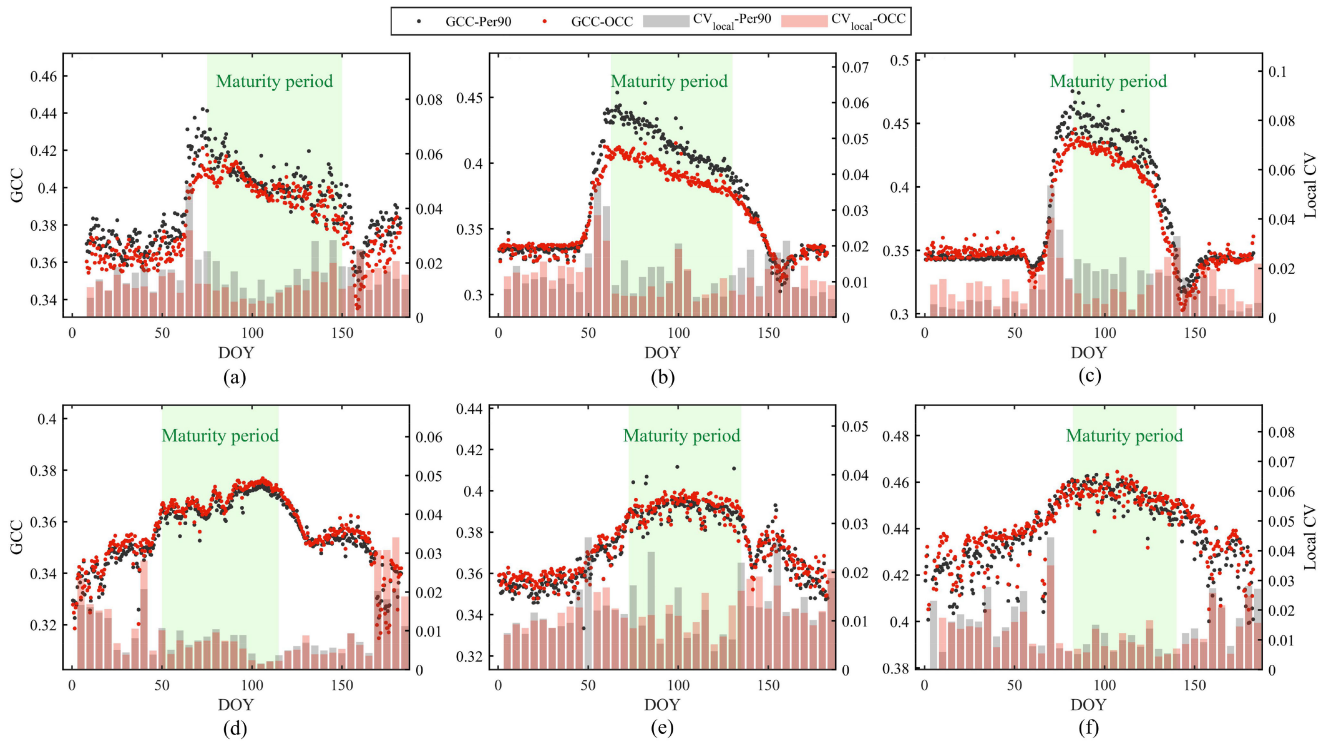


Fig. 9. GCC<sub>Per90</sub> and GCC<sub>OCC</sub> time series data and respective local CV at the (a) Millhaft, (b) Alligatorriver, (c) Bartlettir, (d) OregonMP, (e) Howland1, and (f) Niwot2 sites. The maturity period is marked with a light-green background color.

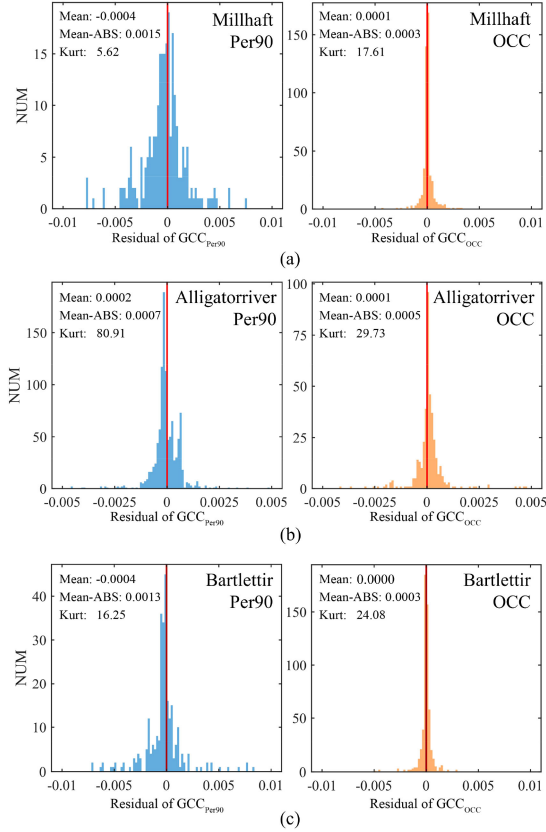


Fig. 10. Histogram distribution of residuals between GCC time series generated from the resampled and original datasets for sites dominantly influenced by varying atmospheric conditions.

observations at high solar angles have less impact on  $GCC_{OCC}$  than on  $GCC_{Per90}$ . Hence, the proposed method can be considered insensitive to seasonal changes in solar angle, although both  $GCC_{OCC}$  and  $GCC_{Per90}$  time series were comparably smooth.

#### IV. DISCUSSION

##### A. Improved Robustness to Varying Illumination Conditions

The superiority of the proposed method can be attributed to the full exploitation of the effective observation under good illumination conditions. The color of sunlit pixels is generally closer to the true color than shaded pixels because of the relatively linear response under good illumination conditions for consumer-grade cameras. However, the traditional Per90 filter can miss sunny photographs because the shaded pixels could have higher GCC values in certain cases owing to color distortion. Herein, we investigated the proportions of sunny and cloudy photographs selected by the Per90 method and used the OCC method (Fig. 12). As shown in Fig. 12(a)–(c), the proportion of sunny photographs selected by the Per90 method at the three sites was only 18.1%, 44.7%, and 17.5%, respectively. Such an inclination to select cloudy photographs will lead to a color distortion in the daily photographs generated and high noise in the GCC time series. Contrastingly, the proportion of sunny photographs used in the proposed OCC method was relatively higher [see Fig. 12(d)–(f)], indicating that the proposed

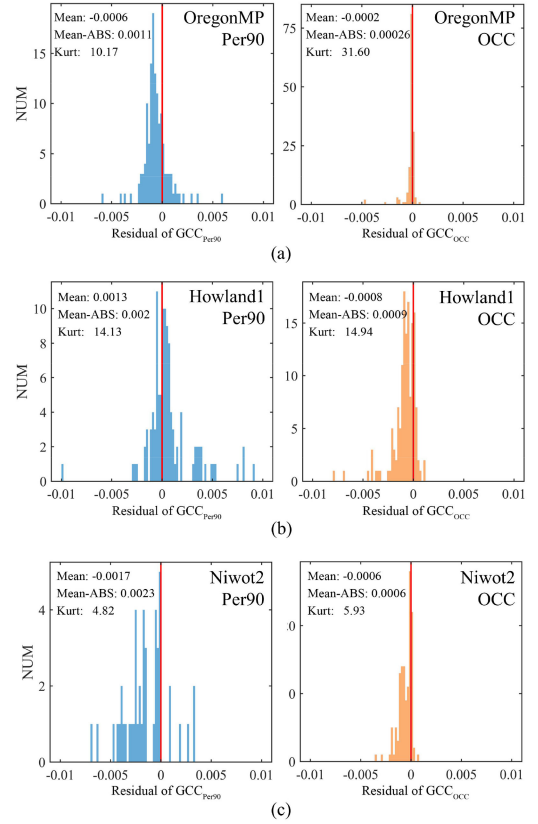


Fig. 11. Histogram distribution of residuals between GCC time series generated from the resampled and original datasets for the sites dominantly influenced by varying solar angles.

method can select more sunlit pixels with good illumination and reduce the interference of cloudy pixels. As the atmospheric condition typically changes extremely quickly, the OCC method can generate more stable GCC curves by removing the dark pixels induced by cloudy weather.

Seasonal and diurnal changes in the solar angle infer the GCC value in a smoother manner; thus, the two methods produce comparably smooth GCC curves for the three sites where the varying solar angle dominates the GCC uncertainty [see Fig. 9(d)–(f)]. Because a seasonal solar change is largely consistent with seasonal color change in vegetation, the GCC uncertainty induced by solar change is difficult to reflect in the stability of the GCC curves. However, the distribution of capturing time of the photographs selected or used in the two methods can reflect the robustness to varying solar angles in an indirect manner. For the OregonMP, Howland1, and Niwot2 sites, the capturing time of the photographs used in the OCC method ranged evenly from 9:00 to 15:00. The capturing time of the photographs selected by Per90 is largely dependent on specific moments, for example, noon with a high solar angle in the OregonMP and Howland1 sites (see Fig. 13). For the Niwot2 site, photographs captured at 14:30 are more likely to be selected using the Per90 method because there are still many cloudy photographs at noon for this site. As the solar angle at noon changes seasonally throughout the year, the shadow areas of the Per90-photographs also change with the seasonal change in



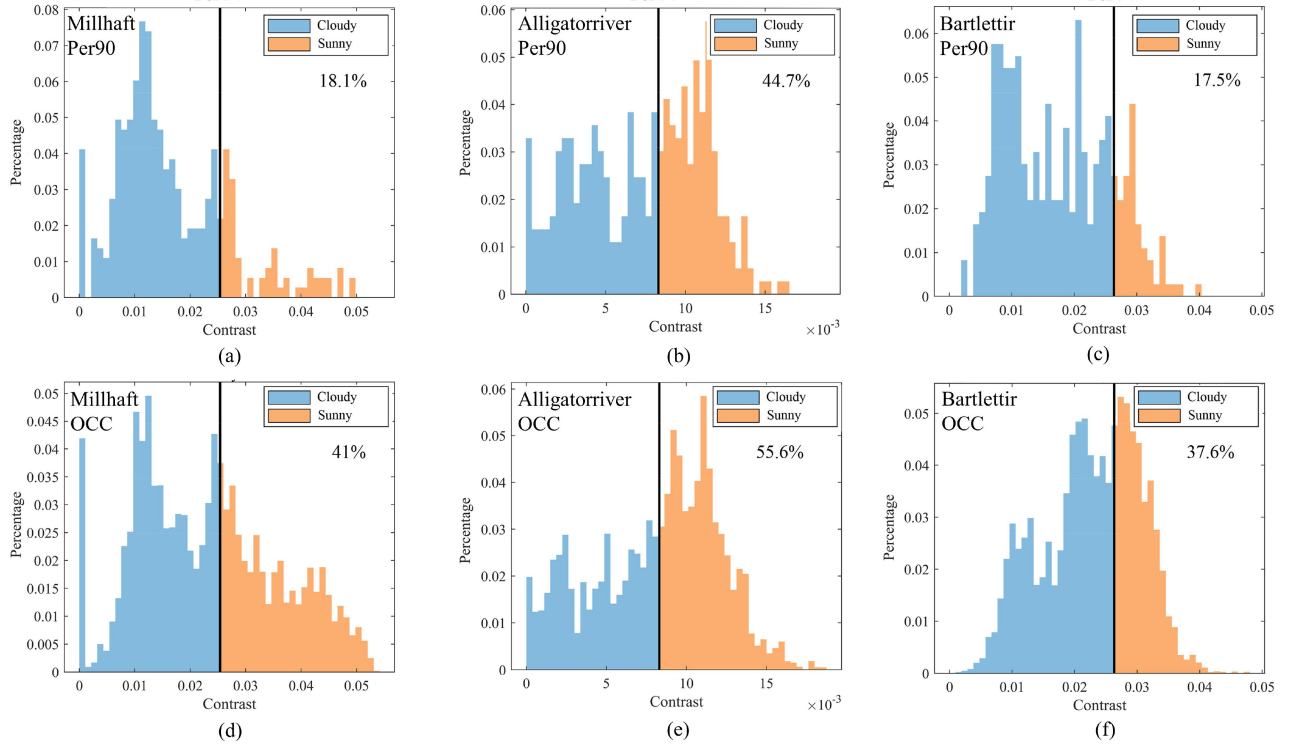


Fig. 12. Histogram distributions of the contrast of photos selected by (a)–(c) Per90 method and (d)–(f) OCC method. The black lines denote the empirical contrast thresholds of sunny photos.

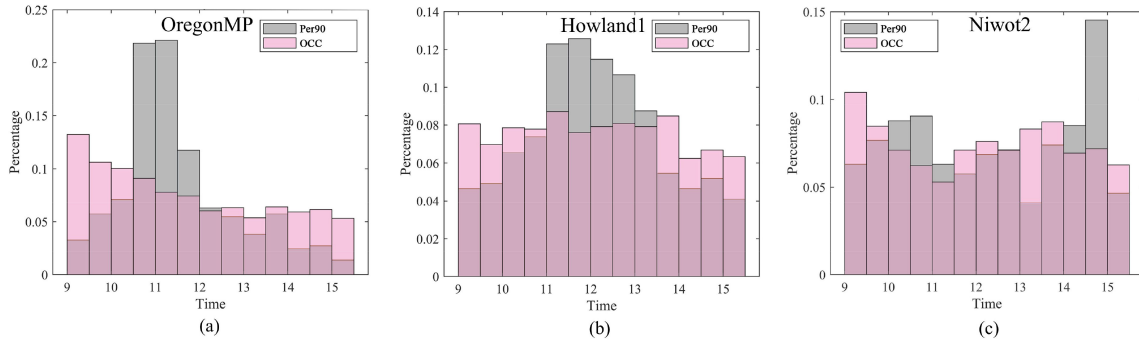


Fig. 13. Histogram of the capturing time of photographs used by OCC method (pink bar) and Per90 method (gray bar) for the sites of (a) OregonMP, (b) Howland1, and (c) Niwot2.

solar angle, which might lead to systematic bias in the  $\text{GCC}_{\text{Per90}}$  time series. However, the proposed OCC method fully exploits the photographs captured under different solar angles throughout a single day; thus, it can be more robust to seasonal changes in the solar angle.

In summary, the composition of optimal DNs acquired under good illumination and a correct exposure setting improves the robustness to varying solar angles and atmospheric conditions by fully exploiting all pixels in all photographs, compared with selecting one photograph each day using the Per90 method.

### B. Selection of Sliding Window Size

In this study, the OCC method selects the optimal DN values and synthesizes virtual photographs through a nonoverlapping

sliding window with a  $3 \times 3$  pixel resolution. However, the optimal size of the sliding window is related to the photographic resolution and canopy structure. To explore the effect of the sliding window size, we varied the window size from a pixel resolution of  $1 \times 1$  to  $10 \times 10$  in the OCC composition. The cumulative local CV of the GCC time series in the maturity season was then used to evaluate the stability of the generated GCC time series. As shown in Fig. 14, the optimal window size corresponding to the lowest cumulative local CV varied from site to site. In general, the optimal window size for the deciduous forest sites, ranging from  $3 \times 3$  to  $5 \times 5$  in pixel resolution, is relatively larger than the optimal window size for conifer forest sites because the nonoverlapping sliding window can help reduce the leaf shadows in the deciduous canopy. However, any window size ranging from a pixel resolution of  $1 \times 1$  to  $4 \times 4$  can

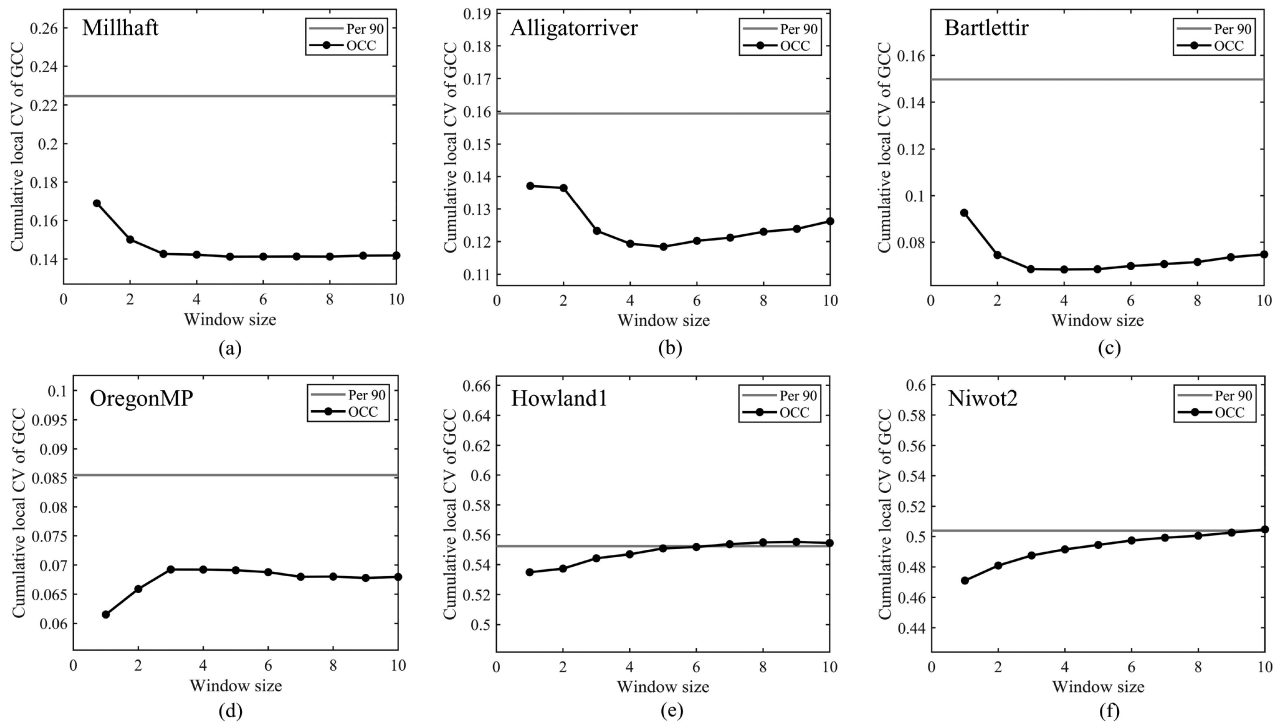


Fig. 14. Cumulative local CV during maturity season for the GCC time series generated through OCC with different nonoverlapping sliding window sizes at the (a) Millhaft, (b) Alligatorriver, (c) Bartlettir, (d) OregonMP, (e) Howland1, and (f) Niwot2 sites.

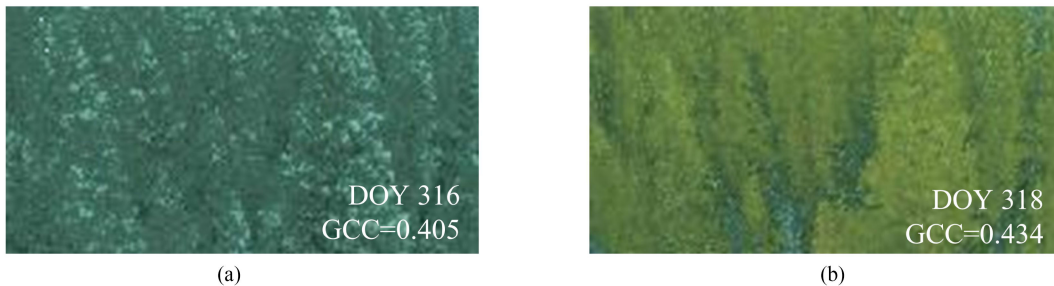


Fig. 15. Comparison of photographs generated by OCC on the days (a) with and (b) without snow-cover.

generate an adequately stable GCC time series with a smaller local CV compared to the Per90 method for all six sites. This indicates that the window size is not a sensitive parameter for generating a stable GCC time series. Notably, a large window size reduces the spatial resolution of the composite photographs. For the application of textural features in the photographs, a small window with a pixel resolution of  $1 \times 1$  is preferred to maintain the original spatial resolution. In summary, a window pixel resolution of  $1 \times 1$  or  $3 \times 3$  can satisfy the requirements of most applications.

### C. Limitations

Although the proposed OCC method shows less sensitivity to varying illumination conditions compared to the commonly used Per90 filter, the OCC method suffers from three limitations. First, the fluctuation induced by the snow-covered pixels in the nongrowing season is more serious in the proposed method than

in the Per90 method. In this study, although the snow pixels were removed using an empirical criterion, the remaining snow pixels largely reduced the GCC (see Fig. 15). Although the snow effect also exists for the Per90 method, such an impact is slight because the Per90 filter is a general statistical criterion that reduces all types of noise. In fact, removing the pixels under the three particular conditions (snow-covered, excessively blue, and direct sunlight exposure) did not affect the Per90 filtered GCC time series (see Fig. S6, Supplementary Material). Contrastingly, the proposed method can only suppress the effect of the illumination variation. Therefore, a more advanced method is required to address the snow effect when using the proposed method on snow-covered sites. Second, the proposed OCC method is a composition method rather than a correction method. Thus, a cloudy GCC cannot be corrected to a sunny GCC in the case of continuous cloudy weather throughout the day because of the lack of well-illuminated pixels. Third, although the proposed OCC method generated a more stable GCC time series during the

maturity period compared to the Per90 filter, a slight improvement was achieved during the fast transition period of a green-up and colorization. Thus, the key phenological dates, such as the start or end of the season, derived by these two methods might be similar. However, the proposed method might show superiority over other applications, such as monitoring the disturbance or stress during the maturity period.

#### D. Application Potentials

The stable GCC time series and high-quality daily composite photographic sequences generated when applying the OCC method have significant potential in various fields of application.

The vegetation index time series derived from PhenoCam not only can be applied to identify the phenological transition date but can also be used as an important input for ecological modeling. For example, the greenness indices calculated from PhenoCam photographs were input into ecological models for a gross primary production estimation [44], and the excess green index calculated from PhenoCam photographs was also used in previous studies as a surrogate for the fraction of absorbed photosynthetically active radiation [30]. The GCC time series is also used for monitoring the disturbance or stress of vegetation during the maturity period [28], [29], [45]. A stable GCC time series generated by the OCC method can benefit these quantitative applications.

In addition, the daily high-quality photographic sequences generated using the OCC method can reflect not only the color changes but also the structural or morphological changes in the vegetation canopy. With advances in image analysis techniques and high-resolution cameras, more textural information in photographs obtained by PhenoCam can be explored and contributed to different agricultural and ecological applications. For example, Apolo *et al.* used convolutional neural networks to estimate the size and yield of citrus fruits from high-resolution RGB photographs obtained by unmanned aerial vehicles [46]. In addition, Taghavi *et al.* proposed the use of a continuous neural network long short-term memory framework for temporal phenotype/genotype classification based on high-resolution photographs [47]. Chen *et al.* also dissected the phenotypic components of crop plant growth and drought responses based on high-resolution images [48]. High-resolution photographs can also be applied to plant disease detection based on deep learning [49], [50]. Therefore, the high-resolution photo sequences generated using the OCC method can extend the potential application of PhenoCam data to identify the vegetation parameters related to morphological characteristics.

#### V. CONCLUSION

In this article, we designed an OCC method to address the issue of color distortion in PhenoCam photographs induced through varying illumination conditions and nonlinear responses to incoming light. Based on the color brightness and saturation of each pixel, daily photographs were composited by selecting DN<sub>s</sub> acquired during the optimal time with good illumination conditions and correct exposure without the need for any other ancillary data. The experimental results show that the proposed

method can effectively generate a high-quality photographic time series with stable color, from which the derived GCC time series is relatively insensitive to varying illumination conditions. Therefore, the daily photographic time series generated by OCC has a better potential to indicate the seasonal changes in the biochemical and biophysical parameters of leaves, consequently benefiting the application of PhenoCam data.

#### ACKNOWLEDGMENT

The authors would like to thank the PIs and technicians of the PhenoCam sites for their efforts in support of PhenoCam. The development of PhenoCam has been funded by the Northeastern States Research Cooperative, NSF's Macrosystems Biology Program under Award EF-1065029 and Award EF-1702697, and DOE's Regional and Global Climate Modeling Program under Award DE-SC0016011. They would also like to thank the USDA Forest Service Air Resource Management Program and the National Park Service Air Resources Program for contributing their camera imagery to the PhenoCam archive.

#### REFERENCES

- [1] A. D. Richardson, T. F. Keenan, M. Migliavacca, Y. Ryu, O. Sonnentag, and M. Toomey, "Climate change, phenology, and phenological control of vegetation feedbacks to the climate system," *Agric. Forest Meteorol.*, vol. 169, pp. 156–173, Feb. 2013.
- [2] A. Menzel, "Phenology: Its importance to the global change community," *Climatic Change*, vol. 54, no. 4, pp. 379–385, Sep. 2002.
- [3] L. Guo, N. An, and K. Wang, "Reconciling the discrepancy in ground- and satellite-observed trends in the spring phenology of winter wheat in China from 1993 to 2008," *J. Geophys. Res.*, vol. 121, no. 3, pp. 1027–1042, Feb. 2016.
- [4] S. Piao *et al.*, "Plant phenology and global climate change: Current progresses and challenges," *Glob. Change Biol.*, vol. 25, no. 6, pp. 1922–1940, Jun. 2019.
- [5] J. Clark, J. Melillo, J. Mohan, and C. Salk, "The seasonal timing of warming that controls onset of the growing season," *Glob. Change Biol.*, vol. 20, no. 4, pp. 1136–1145, Apr. 2013.
- [6] X. Chen *et al.*, "Does any phenological event defined by remote sensing deserve particular attention? An examination of spring phenology of winter wheat in northern China," *Ecol. Indicators*, vol. 116, Sep. 2020, Art. no. 106456.
- [7] T. Qiu, C. Song, J. S. Clark, B. Seyednasrollah, N. Rathnayaka, and J. Li, "Understanding the continuous phenological development at daily time step with a Bayesian hierarchical space-time model: Impacts of climate change and extreme weather events," *Remote Sens. Environ.*, vol. 247, Sep. 2020, Art. no. 111956.
- [8] J. J. Walker, K. M. de Beurs, and R. H. Wynne, "Dryland vegetation phenology across an elevation gradient in Arizona, USA, investigated with fused MODIS and Landsat data," *Remote Sens. Environ.*, vol. 144, pp. 85–97, Mar. 2014.
- [9] F. Gao *et al.*, "Toward mapping crop progress at field scales through fusion of Landsat and MODIS imagery," *Remote Sens. Environ.*, vol. 188, pp. 9–25, Jan. 2017.
- [10] C. Wang *et al.*, "A snow-free vegetation index for improved monitoring of vegetation spring green-up date in deciduous ecosystems," *Remote Sens. Environ.*, vol. 196, pp. 1–12, Jul. 2017.
- [11] R. Cao, M. Shen, J. Zhou, and J. Chen, "Modeling vegetation green-up dates across the Tibetan plateau by including both seasonal and daily temperature and precipitation," *Agric. Forest Meteorol.*, vol. 249, pp. 176–186, Feb. 2018.
- [12] D. Peng, X. Zhang, B. Zhang, and L. Liu, "Scaling effects on spring phenology detections from MODIS data at multiple spatial resolutions over the contiguous United States," *ISPRS J. Photogramm. Remote Sens.*, vol. 132, pp. 185–198, Oct. 2017.
- [13] X. Chen, D. Wang, J. Chen, C. Wang, and M. Shen, "The mixed pixel effect in land surface phenology: A simulation study," *Remote Sens. Environ.*, vol. 211, pp. 338–344, Jun. 2018.



- [14] L. Liu, R. Cao, M. Shen, J. Chen, J. Wang, and X. Zhang, "How does scale effect influence spring vegetation phenology estimated from satellite-derived vegetation indexes?" *Remote Sens.*, vol. 11, no. 18, Sep. 2019, Art. no. 2137.
- [15] L. Zeng, B. D. Wardlow, D. Xiang, S. Hu, and D. Li, "A review of vegetation phenological metrics extraction using time-series, multispectral satellite data," *Remote Sens. Environ.*, vol. 237, Nov. 2019, Art. no. 111511.
- [16] A. D. Richardson, B. H. Braswell, D. Y. Hollinger, J. P. Jenkins, and S. V. Ollinger, "Near-surface remote sensing of spatial and temporal variation in canopy phenology," *Ecol. Appl.*, vol. 19, no. 6, pp. 1417–1428, Sep. 2009.
- [17] L. Wingate *et al.*, "Interpreting canopy development and physiology using the EUROPhen camera network at flux sites," *Biogeosci. Discuss.*, vol. 12, pp. 7979–8034, May 2015.
- [18] K. N. Nasahara and S. Nagai, "Review: Development of an in situ observation network for terrestrial ecological remote sensing: The phenological eyes network (PEN)," *Ecol. Res.*, vol. 30, pp. 211–223, Jan. 2015.
- [19] A. Richardson *et al.*, "Tracking vegetation phenology across diverse North American biomes using phenocam imagery," *Sci. Data*, vol. 5, no. 4, Mar. 2018, Art. no. 180028.
- [20] C. A. Polgar and R. B. Primack, "Leaf-out phenology of temperate woody plants: From trees to ecosystems," *New Phytologist*, vol. 191, pp. 926–941, Sep. 2011.
- [21] T. B. Brown *et al.*, "Using phenocams to monitor our changing earth: Toward a global phenocam network," *Front. Ecol. Environ.*, vol. 14, no. 2, pp. 84–93, Mar. 2016.
- [22] L. P. C. Morellato *et al.*, "Linking plant phenology to conservation biology," *Biol. Conservation*, vol. 195, pp. 60–72, Mar. 2016.
- [23] T. F. Keenan and A. D. Richardson, "The timing of autumn senescence is affected by the timing of spring phenology: Implications for predictive models," *Glob. Change Biol.*, vol. 21, no. 7, pp. 2634–2641, Jul. 2015.
- [24] S. T. Klosterman *et al.*, "Evaluating remote sensing of deciduous forest phenology at multiple spatial scales using phenocam imagery," *Biogeosciences*, vol. 11, no. 16, pp. 4305–4320, Aug. 2014.
- [25] V. F. Rodriguez-Galiano, J. Dash, and P. M. Atkinson, "Intercomparison of satellite sensor land surface phenology and ground phenology in Europe," *Geophys. Res. Lett.*, vol. 42, no. 7, pp. 2253–2260, Apr. 2015.
- [26] X. Zhang *et al.*, "Evaluation of land surface phenology from VIIRS data using time series of phenocam imagery," *Agric. Forest Meteorol.*, vol. 256/257, pp. 137–149, Jun. 2018.
- [27] S. H. Knox *et al.*, "Using digital camera and landsat imagery with eddy covariance data to model gross primary production in restored wetlands," *Agric. Forest Meteorol.*, vol. 237/238, pp. 233–245, May 2017.
- [28] Y. Zhou *et al.*, "Examining the short-term impacts of diverse management practices on plant phenology and carbon fluxes of old world bluestem pasture," *Agric. Forest Meteorol.*, vol. 237/238, pp. 60–70, May 2017.
- [29] R. Zhou *et al.*, "Relationship between gross primary production and canopy colour indices from digital camera images in a rubber (*Hevea brasiliensis*) plantation, southwest China," *Forest Ecol. Manage.*, vol. 437, pp. 222–231, Apr. 2019.
- [30] M. Migliavacca *et al.*, "Using digital repeat photography and eddy covariance data to model grassland phenology and photosynthetic CO<sub>2</sub> uptake," *Agric. Forest Meteorol.*, vol. 151, no. 10, pp. 1325–1337, Oct. 2011.
- [31] X. Yang, J. Tang, and J. F. Mustard, "Beyond leaf color: Comparing camera-based phenological metrics with leaf biochemical, biophysical, and spectral properties throughout the growing season of a temperate deciduous forest," *J. Geophys. Res.*, vol. 119, no. 3, pp. 181–191, Mar. 2014.
- [32] C. G. Andresen, C. E. Tweedie, and V. L. Loughheed, "Climate and nutrient effects on Arctic wetland plant phenology observed from phenocams," *Remote Sens. Environ.*, vol. 205, pp. 45–55, Feb. 2018.
- [33] A. D. Richardson, J. P. Jenkins, B. H. Braswell, D. Y. Hollinger, S. V. Ollinger, and M.-L. Smith, "Use of digital webcam images to track spring green-up in a deciduous broadleaf forest," *Oecologia*, vol. 152, pp. 323–334, Mar. 2007.
- [34] O. Sonnentag *et al.*, "Digital repeat photography for phenological research in forest ecosystems," *Agric. Forest Meteorol.*, vol. 152, pp. 159–177, Jan. 2012.
- [35] T. Julitta *et al.*, "Using digital camera images to analyse snowmelt and phenology of a subalpine grassland," *Agric. Forest Meteorol.*, vol. 198/199, pp. 116–125, Nov./Dec. 2014.
- [36] G. Filippa *et al.*, "Phenopix: AR package for image-based vegetation phenology," *Agric. For. Meteorol.*, vol. 220, pp. 141–150, Apr. 2016.
- [37] A. Vrieling *et al.*, "Vegetation phenology from sentinel-2 and field cameras for a Dutch barrier island," *Remote Sens. Environ.*, vol. 215, pp. 517–529, Sep. 2018.
- [38] S. Sunoj, C. Igathinathane, N. Saliendra, J. Hendrickson, and D. Archer, "Color calibration of digital images for agriculture and other applications," *ISPRS J. Photogramm. Remote Sens.*, vol. 146, pp. 221–234, Dec. 2018.
- [39] W. Grey, P. R. J. North, S. Los, and R. Mitchell, "Aerosol optical depth and land surface reflectance from multiangle AATSR measurements: Global validation and intersensor comparisons," *IEEE Trans. Geosci. Remote Sens.*, vol. 44, no. 8, pp. 2184–2197, Aug. 2006.
- [40] N. Hsu, S.-C. Tsay, M. King, and J. Herman, "Aerosol properties over bright-reflecting source regions," *IEEE Trans. Geosci. Remote Sens.*, vol. 42, no. 3, pp. 557–569, Mar. 2004.
- [41] R. Richter, "Atmospheric correction of satellite data with haze removal including a haze/clear transition region," *Comput. Geosci.*, vol. 22, no. 6, pp. 675–681, Jul. 1996.
- [42] T. Popp, "Correcting atmospheric masking to retrieve the spectral albedo of land surfaces from satellite measurements," *Int. J. Remote Sens.*, vol. 16, no. 8, pp. 3483–3508, Dec. 1995.
- [43] A. Smith, "Color gamut transform pairs," *ACM SIGGRAPH Comput. Graph.*, vol. 12, no. 3, pp. 12–19, Aug. 1978.
- [44] D. Yan, R. L. Scott, D. J. P. Moore, J. A. Biederman, and W. K. Smith, "Understanding the relationship between vegetation greenness and productivity across dryland ecosystems through the integration of phenocam, satellite, and eddy covariance data," *Remote Sens. Environ.*, vol. 223, pp. 50–62, Mar. 2019.
- [45] N. B. Gonçalves, A. P. Lopes, R. Dalagnol, J. Wu, D. M. Pinho, and B. W. Nelson, "Both near-surface and satellite remote sensing confirm drought legacy effect on tropical forest leaf phenology after 2015/2016 ENSO drought," *Remote Sens. Environ.*, vol. 237, Feb. 2020, Art. no. 111489.
- [46] O. E. Apolo, J. Martínez Guanter, G. Egea, P. Raja, and M. Pérez-Ruiz, "Deep learning techniques for estimation of the yield and size of citrus fruits using a UAV," *Eur. J. Agron.*, vol. 115, Apr. 2020, Art. no. 126030.
- [47] S. Taghavi, M. Esmailzadeh, M. Najafi, T. Brown, and J. Borevitz, "Deep phenotyping: Deep learning for temporal phenotype/genotype classification," *Plant Methods*, vol. 14, Aug. 2018, Art. no. 66.
- [48] D. Chen *et al.*, "Dissecting the phenotypic components of crop plant growth and drought responses based on high-throughput image analysis," *Plant Cell*, vol. 26, no. 12, pp. 4636–4655, Dec. 2014.
- [49] C. DeChant *et al.*, "Automated identification of northern leaf blight-infected maize plants from field imagery using deep learning," *Phytopathology*, vol. 107, no. 11, pp. 1426–1432, Nov. 2017.
- [50] S. P. Mohanty, D. P. Hughes, and M. Salathé, "Using deep learning for image-based plant disease detection," *Front. Plant Sci.*, vol. 7, Sep. 2016, Art. no. 1419.



**Qing Li** received the B.E. degree in spatial information and digital technology from the University of Electronic Science and Technology of China, Chengdu, China, in 2018. She is currently working toward the master's degree in cartography and geographical information engineering with Beijing Normal University, Beijing, China.

Her research interests include PhenoCam data and vegetation index time series data processing.



**Miaogen Shen** received the B.S. degree in physics and the Ph.D. degree in physical geography from Beijing Normal University, Beijing, China, in 2004 and 2009, respectively.

From 2009 to 2012, he was a Postdoctoral Fellow with the National Institute for Environmental Studies, Tsukuba, Japan, and from 2012 to 2020, he was a Research Professor with the Institute of Tibetan Plateau Research, Chinese Academy of Sciences. He is currently a Professor with the Institute of Land Surface System and Sustainable Development, Faculty of Geographical Science, Beijing Normal University. His research interests include responses and feedback of terrestrial ecosystems to climate change, ecological remote sensing, and plant phenology.



**Xuehong Chen** received the B.S. degree in physics and the M.S. degree in civil engineering from Beijing Normal University, Beijing, China, in 2006 and 2009, respectively, and the Ph.D. degree in earth and environmental science from Nagoya University, Nagoya, Japan, in 2012.

He is currently an Associate Professor with the Institute of Remote Sensing Science and Engineering, Faculty of Geographical Science, Beijing Normal University. His research interests include preprocessing, data fusion of satellite images, and land cover

mapping by remote sensing.



**Xin Cao** received the B.S. and M.S. degrees in geography from Beijing Normal University, Beijing, China, in 2002 and 2005, respectively, and the Ph.D. degree in environmental engineering from Nagoya University, Nagoya, Japan, in 2008.

During 2008–2009, he was a Researcher with Nagoya University. He is currently an Associate Professor with the Institute of Remote Sensing Science and Engineering, Faculty of Geographical Science, Beijing Normal University. His research interests include urban remote sensing and remote sensing

modeling in grassland.



**Cong Wang** received the B.S. degree in physics and the Ph.D. degree in geographical information systems from Beijing Normal University, Beijing, China, in 2011 and 2016, respectively.

He is currently a Research Professor with the Key Laboratory of Agricultural Remote Sensing, Ministry of Agriculture and Rural Affairs/Institute of Agricultural Resources and Regional Planning, Chinese Academy of Agricultural Sciences. His current research interests include agricultural remote sensing, plant phenology, and solar-induced chlorophyll fluorescence.



**Xihong Cui** received the B.S. degree in machinery design & manufacture from Beihang University, Beijing, China, in 1998, and the M.S. and Ph.D. degrees in cartography and geographical information system from Beijing Normal University, Beijing, in 2007 and 2009, respectively.

She is currently an Associate Professor with the Institute of Remote Sensing Science and Engineering, Faculty of Geographical Science, Beijing Normal University. Her research interests include remote sensing and the application of GPR for ecology study.



**Jin Chen** received the B.A. and M.S. degrees in geography from Beijing Normal University, Beijing, China, in 1989 and 1992, respectively, and the Ph.D. degree in civil engineering from Kyushu University, Fukuoka, Japan, in 2000.

He was a Postdoctoral Researcher with the University of California, Berkeley, CA, USA, from 2000 to 2001, and with the National Institute of Environmental Studies, Tsukuba, Japan, from 2001 to 2004. He is currently a Professor with the Institute of Remote Sensing Science and Engineering, Faculty

of Geographical Science, Beijing Normal University. His research interests include remote sensing modeling and vegetation parameter retrieval through the inversion of remote sensing models.